# Concurrent MRI and diffuse optical tomography of breast after indocyanine green enhancement

**Vasilis Ntziachristos*†‡, A. G. Yodh§, Mitchell Schnall¶, and Britton Chance†**

Departments of *Bioengineering, †Biochemistry/Biophysics, §Physics and Astronomy, and ¶Radiology, University of Pennsylvania, Philadelphia, PA 19104-6089

Contributed by Britton Chance, December 23, 1999

**We present quantitative optical images of human breast *in vivo*. The images were obtained by using near-infrared diffuse optical tomography (DOT) after the administration of indocyanine green (ICG) for contrast enhancement. The optical examination was performed concurrently with a magnetic resonance imaging (MRI) exam on patients scheduled for excisional biopsy or surgery so that accurate image coregistration and histopathological information of the suspicious lesions was available. The ICG-enhanced optical images coregistered accurately with Gadolinium-enhanced magnetic resonance images validating the ability of DOT to image breast tissue. In contrast to simple transillumination, we found that DOT provides for localization and quantification of exogenous tissue chromophore concentrations. Additionally our use of ICG, an albumin bound absorbing dye in plasma, demonstrates the potential to differentiate disease based on the quantified enhancement of suspicious lesions.**

optical properties | contrast agents | MRI coregistration

Diffuse optical tomography (DOT) in the near-infrared (NIR) is an emerging imaging modality with potential application in radiology. The technique has the capacity to produce quantitative images of intrinsic and extrinsic absorption and scattering (1–4), as well as fluorophore lifetime and yield (5–7) in diffuse media such as tissue. These fundamental quantities can then be used to derive tissue oxy- and deoxyhemoglobin concentrations, blood oxygen saturation (8), contrast agent uptake, and organelle concentration (9). Such novel contrast mechanisms are important for practical applications such as the measurement of tissue metabolic state, angiogenesis, and permeability for cancer detection (10–12), the measurement of functional activity in brain (13) and muscle (14), and the detection of hematomas (15).

Optical imaging of large organs such as breast is often feasible because of the low absorption of tissue in the 700-to 850-nm spectral region. In fact, light has been investigated since the late 1920s as a diagnostic tool for breast cancer (16–21) by transillumination (also called diaphanography). Transillumination, however, had low spatial resolution and afforded little in spectral quantification of lesions. Hence, it did not attain sufficient sensitivity and specificity to be used clinically (18, 20).

During the last decade, rigorous mathematical modeling of light propagation in tissue, combined with technological advancements in photon sources and detection techniques, has improved transillumination measurements (21, 22) but additionally has made possible the application of tomographic principles (1–3, 23, 24) for imaging with diffuse light. Diffuse optical tomography has dramatically improved our ability to localize and quantify tissue structures with light. Furthermore, the method employs non-ionizing radiation and relatively low cost instrumentation. Its main disadvantage remains the low spatial resolution achieved as a result of the highly scattering nature of tissue in the NIR. The resolution of current experimental DOT implementations (25, 26) is $\approx$5 mm millimeters, although increased numbers of source-detector pairs and improved signal-to-noise may lead to further resolution improvement.

Thus far, DOT images of absorbing and scattering objects embedded in tissue-like media have been produced (2, 25–30) by using phantoms. The experimental certainty of the phantom contrast makes the evaluation of the technique straightforward. *In vivo* measurements, on the other hand, require selection of an appropriate "Gold Standard" for DOT validation in the clinical environment. One way to achieve validation is to compare NIR reconstructions with images from other well established modalities such as x-ray computed tomography, ultrasound, or MRI. MRI is an excellent candidate for this scheme because it provides both structural and functional information.

In this work, we report on *in vivo* diffuse optical tomography of the human breast after contrast agent administration. The contrast agent we employ, indocyanine green (ICG), is an absorber and fluorophore in the NIR that was originally used in liver function studies, angiography, and cardiac output monitoring (31). Here, we consider its utility for absorption-based breast cancer detection using DOT. The optical examination is performed simultaneously with a magnetic resonance (MR) examination protocol after gadolinium (Gd) administration. Surgery or excisional biopsy performed on patients participating in the study provides accurate pathological information about the imaged lesions.

The concurrent examination enables MR and DOT imaging under identical physiological conditions and geometry. The MR and DOT images are accurately coregistered by using specially designed fiducials that mark the position of the optical set-up on the MR images. The use of contrast-enhanced images for both DOT and MRI provides a good validation model based on the functional characteristics of tissue. Additionally the use of contrast agents allows reconstruction of differential images (32) that is minimally affected by experimental uncertainties. Although the simultaneous examination offers the possibility to employ MR structural and functional images as *a priori* information to improve the DOT reconstruction (33, 34), here we only perform a direct comparison of the two modalities as stand-alone methods.

We present three cases: a ductal carcinoma, a fibroadenoma, and a control study with no suspicious enhancement. Our aim was to validate the efficiency of DOT for imaging breast and breast cancer and to demonstrate features of contrast enhanced DOT. The ICG-enhanced images reveal good congruence with the Gd-enhanced MR images. Contrast agent uptake exhibited differentiation between disease and other structures. Thus, the potential usefulness of ICG in diffuse optical mammography was documented, and, more generally, the possibility to use DOT with engineered contrast agents that target cancer or probe specific functionality was demonstrated *in vivo*.

## Methods

**NIR Imager.** Our NIR imager and its performance for resolving absorbing and scattering objects in phantom measurements has

Abbreviations: DOT, diffuse optical tomography; NIR, near-infrared; ICG, indocyanine green; MR, magnetic resonance; Gd, gadolinium; VOI, volume of interest.

‡To whom reprint requests should be addressed at: University of Pennsylvania, D501 Richards Building, 37th and Hamilton Walk, Philadelphia, PA 19104-6089. E-mail: vasilis@mail.med.upenn.edu.

The publication costs of this article were defrayed in part by page charge payment. This article must therefore be hereby marked "*advertisement*" in accordance with 18 U.S.C. §1734 solely to indicate this fact.

Article published online before print: *Proc. Natl. Acad. Sci. USA*, 10.1073/pnas.040570597. Article and publication date are at www.pnas.org/cgi/doi/10.1073/pnas.040570597

been described (26). The instrument operates in the time-domain using time-correlated single photon counting. The measurements are Fourier transformed to produce data at multiple modulation frequencies. The source used in this study was an ≈40 $\mu$W laser diode at 830 nm pulsing at a repetition rate of 5 MHz with a pulse width of 50 ps. The laser source is coupled to 24 source fibers via an optical switch (DiCon Fiberoptics, Berkeley, CA). The detection uses eight fiber bundles and collects photon signals from the breast in parallel. Both source fibers and fiber bundles are 10 m long so that the imager may be placed outside the Faraday cage to avoid interference with the MR scanner. The breast is compressed softly between two plates. The plates hold fibers, radio-frequency coils for MRI, and specially designed fiducials that appear on the MR images for coregistration purposes. All source fibers are mounted on one plate, forming a $3 \times 8$ grid array with adjacent fiber separations of 1.25 cm. All detector fiber bundles are mounted on the other plate, forming a $2 \times 4$ grid array with adjacent fiber separation of 2.5 cm.

**Diffuse Optical Tomography.** Diffuse optical tomography typically requires two mathematical tasks: (*i*) modeling of the photon propagation in the scattering medium (forward problem), and (*ii*) data inversion to reconstruct the images (inverse problem). We have employed the perturbation approach (1, 2, 35) to solve the forward problem in the frequency domain. Here we outline a special formulation of the general reconstruction framework, well suited to imaging the contrast enhanced breast. The details of this formulation and its evaluation are described elsewhere (32). In brief, the absorption ($\mu_a'(\vec{r})$) and diffusion ($D'(\vec{r})$) coefficients of the pre-ICG breast are divided into spatially dependent ($\delta\mu_a'(\vec{r})$, $\delta D'(\vec{r})$) and background components ($\mu_{a0}'$, $D_0'$): i.e., $\mu_a'(\vec{r}) = \mu_{a0}' + \delta\mu_a'(\vec{r})$ and $D'(\vec{r}) = D_0' + \delta D'(\vec{r})$. After the Rytov expansion (35), the photon density (total field) wave with modulation frequency $\omega$, measured at position $\vec{r}_d$ due to a source at position $\vec{r}_s$ can be written as the product of two terms: i.e.,

$$U'(\vec{r}_s, \vec{r}_d, \omega) = U_0'(\vec{r}_s, \vec{r}_d, \omega)e^{\phi_{sc}'(\vec{r}_s,\vec{r}_d,\omega)}, \qquad [1]$$

where the scattered field $\phi_{sc}'(\vec{r}_s, \vec{r}_d, \omega)$ is the field component scattered from the existing heterogeneity ($\delta\mu_a'(\vec{r})$,$\delta D'(\vec{r})$) and the incident field $U_0'(\vec{r}_s,\vec{r}_d, \omega)$ is the field that would have been detected from the same medium if these heterogeneities were not present. After the administration of a contrast agent, the background optical properties change, and the total field is

$$U''(\vec{r}_s, \vec{r}_d, \omega) = U_0''(\vec{r}_s, \vec{r}_d, \omega)e^{\phi_{sc}''(\vec{r}_s,\vec{r}_d,\omega)}, \qquad [2]$$

where $\phi_{sc}'$ $(\vec{r}_s, \vec{r}_d, \omega)$ is the field component scattered from the post-ICG heterogeneity [i.e., $\delta\mu_a''(\vec{r})$, $\delta D''$ $(\vec{r})$ with respect to the new background optical properties $\mu_{a0}''$, $D_0''$] and $U_0''(\vec{r}_s, \vec{r}_d,\omega)$ is the incident field obtained from a homogeneous medium with $\mu_{a0}''$, $D_0''$. Combining Eq. **1** with Eq. **2**, we obtain the relative scattered field: i.e.,

$$\phi_{sc} = \phi_{sc}'' - \phi_{sc}' = \ln\left(\frac{U''}{U'} \cdot \frac{U_0'}{U_0''}\right), \qquad [3]$$

which is the field scattered from the perturbations created by the contrast agent injection. It can be shown (32) by using first order perturbation theory that

$$\phi_{sc}(\vec{r}_s, \vec{r}_d, \omega) \cong -\int_V [W^a(\vec{r}, \mu_{a0}'', D_0'', \omega)\delta\mu_a^{\mathrm{ICG}}(\vec{r}) + W^s(\vec{r}, \mu_{a0}'', D_0'', \omega)\delta D^{\mathrm{ICG}}(\vec{r})]d\vec{r}, \qquad [4]$$

where $W^a$ ($W^s$) represents the absorption (scattering) weights of perturbations at position $\vec{r}$, due to a source at $\vec{r}_s$ and a detector at $\vec{r}_d$. $\delta\mu_a^{\mathrm{ICG}}(\vec{r})$, $\delta D^{\mathrm{ICG}}(\vec{r})$ are the unknown "differential" perturbations of the absorption and diffusion coefficient arising from the contrast agent distribution alone. The approximations leading to Eq. **4** work particularly well for transmittance geometry where $|\vec{r}_s - \vec{r}_d| \approx |\vec{r}_s - \vec{r}| + |\vec{r} - \vec{r}_d|$ for the most probable photon paths between $\vec{r}_s$ and $\vec{r}_d$; they also work well when $\delta\mu_a'(\vec{r})$, $\delta D'(\vec{r})$ are small (32). The exact form for the weights is given elsewhere (32). The transmittance geometry is implemented assuming the method of image sources (36). For image reconstruction, this integral equation is discretized into a sum of volume elements (voxels), and the scattered field is obtained for every source-detector pair and employed frequency $\omega$. For $n$ voxels and $m = o \times p \times q$ measurements, where $o$ is the number of sources, $p$ is the number of detectors, and $q$ is the number of frequencies employed, the discretization yields a set of coupled linear equations

$$\begin{bmatrix} \phi_{sc}^1(\vec{r}_{s1}, \vec{r}_{d1}, \omega_1) \\ \vdots \\ \phi_{sc}^m(\vec{r}_{so}, \vec{r}_{dp}, \omega_q) \end{bmatrix} \qquad [5]$$

$$= \begin{bmatrix} W_{11}^a & \cdots & W_{1n}^a & W_{11}^s & \cdots & W_{1n}^s \\ \vdots & \ddots & \vdots & \vdots & \ddots & \vdots \\ W_{m1}^a & \cdots & W_{mn}^a & W_{m1}^s & \cdots & W_{mn}^s \end{bmatrix} \cdot \begin{bmatrix} \delta\mu_a^{\mathrm{ICG}}(\vec{r}_1) \\ \vdots \\ \delta\mu_a^{\mathrm{ICG}}(\vec{r}_n) \\ \delta D^{\mathrm{ICG}}(\vec{r}_1) \\ \vdots \\ \delta D^{\mathrm{ICG}}(\vec{r}_n) \end{bmatrix}.$$

Inverting the weights' matrix determines the spatial map of differential perturbations in absorption and diffusion coefficient due to contrast agent injection.

The reconstructions performed in this study use five frequencies (80, 160, 240, 320, and 400 MHz). Matrix inversion is based on the algebraic reconstruction technique (37) with relaxation parameter $\lambda = 0.1$ and 500 iteration steps. The number of iterations was chosen after calibrating the algorithm with phantom measurements and was kept constant for all cases. Because minimal change in the scattering properties of the breast is expected after ICG injection, we set the diffusion coefficient differential perturbations to zero. Furthermore, to facilitate quantitative comparisons between the DOT images obtained from different patients, we have chosen to reconstruct similar volumes and have kept the voxel size constant: i.e., $0.3 \times 0.4 \times 1$ cm (3). All reconstructions shown are done for a 1-cm-thick slice, perpendicular to the compression plates (coronal plane), passing through the suspicious lesion. Only the real part of Eq. **5** was inverted because it has generally better signal to noise ratio characteristics than the imaginary part.

**Magnetic Resonance Imaging.** MR studies were performed with a 1.5 T imager (Signa, GE Medical Systems, Milwaukee, WI), version 5.4 software. The body coil was used as the transmitter, and a custom-built multicoil consisting of four coils constructed on the two compression plates (38) served as a receiver.

**Examination Protocol.** The simultaneous MR and DOT study and informed consent form were approved by the institutional review board, and the investigation was conducted in full compliance with the accepted standards for research involving humans. Except for control cases, patients entering the study had a previous suspicious mammogram or palpable lesion and were scheduled for excisional biopsy or surgery. Written informed consent was obtained from all participants.

Patient placement followed standard procedures used for the MR examination. The patient assumed the prone position with the breasts falling away from the chest wall and into an H-shaped coil holder. The two compression plates were positioned parallel to the sagittal plane and ensured contact of the optical fibers onto the tissue.

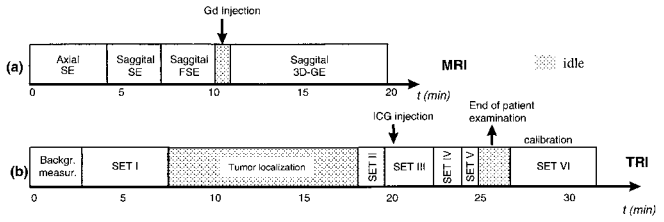


**Fig. 1.** MRI-DOT examination protocol.

The simultaneous examination protocol is depicted in Fig. 1. The MR imaging protocol consisted of (*i*) an axial T1 SE (TR/TE 500/14 FOV 24) localizer, (*ii*) a sagittal T1-weighted SE (TR/TE 500/14 FOV 16), (*iii*) a sagittal T2-weighted, fat-saturated FSE (TR/TE 5000/120 FOV 16), and (*iv*) a sagittal three-dimensional, fat-saturated GRE sequence (TR/TI/TE 9.3/27/2.2, acquisition matrix 512 × 512 FOV 16 slice thickness 2.5–3). The last sequence (*iv*) acquired one pre-Gd and three post-Gd sets of images to investigate the Gd distribution. Gadolinium was administered intravenously at 0.1 mmol/kg.

The DOT examination protocol had two parts. The first part ran simultaneously with the MR protocol. First a measurement with the laser light off was performed to obtain dark current and background light noise. Then the light power was adjusted, and all sources were scanned to obtain the breast baseline (SET I). During the post-Gd period, the DOT protocol selected six sources close to the suspicious region and scanned them during SET II. This measurement acquired the total field $U'(\vec{r}_s, \vec{r}_d, \omega)$ of Eq. **1**. The selection of the sources was based on the information for suspicious lesions produced by the postgadolinium MR images. At the end of the MRI protocol, the first optical source of the chosen six was selected to continuously acquire data at ≈20-s intervals (SET III). Then a bolus of sterile ICG (SERB, Paris, France) was injected intravenously at 0.25 mg/kg. Three minutes after injection, a scan of the remaining 5 sources was performed (SET IV). Finally the input light was directed again to the first source for an additional 1 min of data acquisition at ≈20-s intervals (SET V). The measurements of SET IV and the first measurement of SET V acquire the total field $U''(\vec{r}_s, \vec{r}_d, \omega)$ of Eq. **2**. The overall examination lasted 25 min (20 min for MRI/DOT and 5 min for ICG-enhanced DOT). At the end of the examination protocol, a calibration optical measurement was acquired for all sources on a specially constructed resin model with typical optical properties and dimensions of a human breast (SET VI) that can be used in combination with SET I to image intrinsic breast optical properties.

**NIR Data Preprocessing.** Data preprocessing consisted of three steps:

(*i*) During the first step, standard median filtering was applied to all time resolved curves, followed by subtraction of the dark current and ambient light photon count (obtained before SET I).

(*ii*) In the second step, a correction was effectively applied to the total field $U''(\vec{r}_s, \vec{r}_d, \omega)$ to account for the $\mu''_{a0}$ change as a function of time because of the clearance of ICG from the plasma. This normalization is critical because different sources are "on" at different times whereas ICG is clearing. Fig. 2 shows the average change in $\mu''_{a0}$ from a 50-year-old patient after ICG administration. The measurement is obtained during SET III and SET V for a single source-detector pair. The $\mu''_{a0}$ change calculation is based on an algorithm (39) developed specifically to monitor absorption changes with an accuracy of $10^{-3}$ cm$^{-1}$. The area in gray indicates the time allocated to SET IV. The correction normalizes all data acquired during SET IV to correspond to the absorption level of the first point of SET V. For this purpose, the absorption coefficient $\mu''_{a0}(i)$ ($i = 1 \ldots 5$) was calculated at each of the five time points during SET IV (i.e., the open circles in Fig. 2) by using linear interpolation between the last points of SET III and the first points

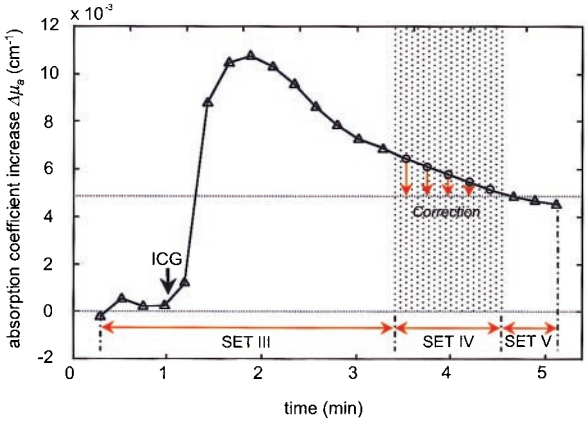


**Fig. 2.** Absorption increase of human breast attributable to ICG injection as a function of time and the correction applied.

of SET V. Each circle defines the temporal midpoint of the acquisition period allocated to a particular source. Although the ICG clearance from the plasma follows an exponential decay, linear interpolation suffices to predict the $\mu_a$ values for the small time interval of SET IV. The $\mu_a(i)$ at each of the points was used to derive a signal intensity $T_i = T_i(t, \mu''_{a0}(i), D''_0, |\vec{r}_s - \vec{r}_d|)$ using the time-domain diffusion equation solution for slab geometry (36). Then, letting $T_6$ be the calculated intensity for the first point of SET V with absorption coefficient $\mu''_{a0}(6)$, five correction factors $a_i$ were calculated; $a_i = max(T_6)/max(T_i)$. The $a_i$ were multiplied with the amplitude of the time-resolved curves $T_i$ acquired at each point $i$. The calculation was done for each patient separately by constructing a graph like the one of Fig. 2.

(*iii*) The third step calculated the relative scattered field $\phi_{sc}$ in Eq. **3**, at each frequency $\omega$. The total fields $U''(\vec{r}_s, \vec{r}_d, \omega)$ and $U'(\vec{r}_s, \vec{r}_d, \omega)$ were obtained at each frequency $\omega$ by Fourier transforming the time resolved curves of SET II and the corrected time-resolved curves of SET IV respectively. The incident fields $U''_0(\vec{r}_s, \vec{r}_d, \omega)$, $U'_0(\vec{r}_s, \vec{r}_d, \omega)$, were theoretically obtained by using the frequency-dependent solution of the diffusion equation (40) for an infinite slab using the post-ICG ($\mu''_{a0}$, $D''_0$) and pre-ICG ($\mu'_{a0}$, $D'_0$) background optical properties. The values $\mu''_{a0}$, $D''_0$ and $\mu'_{a0}$, $D'_0$ were calculated by averaging the optical properties obtained after fitting (39) the time-resolved curves acquired during SET IV and SET II, respectively, to the time-domain diffusion equation for an infinite slab (36).

**Coregistration.** Coregistration is based on the $H_2O$-$CuSO_4$-filled fiducials mounted on the compression plates that appear on the MR images as bright spots. The center of the fiducials was retrieved via image postprocessing on the GRE images that offer the highest resolution of the study. Then the exact three-dimensional position of the sources and detectors relative to the breast is retrieved by simple geometrical calculations.

## Results

Three cases are presented: a malignant tumor, a benign tumor, and a control measurement from a patient with no disease. Average background optical properties and the average absorption increase 3 min after the administration of the contrast agent are tabulated in Table 1 for all cases.

**Case I: Infiltrating Ductal Carcinoma.** Fig. 3 depicts the results from a 70-year-old patient with an infiltrating ductal carcinoma of ≈1 cm. Fig. 3*a* depicts the pre-Gd sagittal MR slice passing through the carcinoma in grayscale and the relative signal increase due to Gd superimposed in color. The color image is obtained by subtracting the corresponding pre-Gd from the post-Gd slice and thresholding

**Table 1. Average optical properties for the three cases studied at 830 nm**

| | $\mu_a$ (cm$^{-1}$) pre-ICG | $\Delta\mu_a$ (cm$^{-1}$) attributable to ICG | $\mu_s'$ (cm$^{-1}$) |
|---|---|---|---|
| Case I | 0.031 ± 0.002 | 0.007 ± 0.001 | 11.1 ± 0.7 |
| Case II | 0.046 ± 0.003 | 0.004 ± 0.001 | 11.9 ± 0.7 |
| Case III | 0.052 ± 0.003 | 0.005 ± 0.001 | 9.3 ± 0.6 |

the resulting image to 40% of the maximum. All of the MR images were median-filtered to reduce shot noise. The rectangle surrounding the carcinoma indicates the sagittal cut of the volume of interest (VOI) imaged under the NIR protocol examination after ICG administration (SET II and SET IV). Fig. 3*b* shows the DOT image obtained from the VOI, along the coronal plane. Fig. 3*c* depicts a pre-Gd GRE coronal slice (in grayscale) passing through the center of the VOI, superimposed with the distribution of Gd (in color) from the entire VOI projected on this coronal plane. The Gd distribution is calculated as $Gd_{VOI} = \Sigma_{i\in VOI}\,[Gd_i^{post}] - [Gd_i^{pre}]$, where $[Gd_i^{post}]$ is the $i$th post-Gd coronal slice that is included in the VOI and $[Gd_i^{pre}]$ the corresponding pre-Gd slice. The final $Gd_{VOI}$ image seen superimposed in color on Fig. 3*c* is thresholded to 40% of the maximum. All post-Gd images used are from the MR set obtained immediately after Gd-chelate injection.

Fig. 3*b* exhibits a marked absorption increase in the upper right of the image, congruent with the position that the carcinoma appears in Fig. 3*c*. The local absorption coefficient increase of this lesion is ≈0.05 cm$^{-1}$ at 830 nm, corresponding to an ICG concentration of ≈0.1 mg/liter. There is another lesion shown in the left part of the NIR image, congruent with enhancements seen on the MR images, albeit with a different size and shape than the MRI lesions. In its current implementation, the low resolution of DOT is not sufficient to separately resolve such small lesions. Furthermore, a characteristic feature of DOT is that there are no clear borders of the structures imaged. Therefore, characterization of a lesion size depends on a selected threshold. The full width at half maximum of the DOT-resolved carcinoma is comparable with the carcinoma size seen on the MRI image. There is fair comparison between the full-width at half-maximum size of the secondary lesion on the DOT image and the corresponding enhancement distribution seen on the MR image. The cancerous lesion, however, shows marked enhancement relative to the secondary structure on the DOT image. One other small absorbing lesion appears on the border of the DOT image. This lesion could be caused by a superficial blood vessel just in front of the corresponding source but is most likely an artifact caused by experimental noise since it does not appear on the Gd image.

**Case II: Fibroadenoma.** Fig. 4 depicts results from a patient diagnosed with a fibroadenoma. The fibroadenoma was 1.5 cm in diameter and was close to one of the two compression plates. The lesion is clearly shown enhanced on the functional MR images of Fig. 4*a* and *c* (produced like Fig. 3 *a* and *c*, respectively). Fig. 4*b* depicts the result obtained with DOT for the VOI. There is a lesion that appears mildly enhanced after ICG injection congruent with the appearance of the fibroadenoma on Fig. 4*c*. The $\Delta\mu_a$ value reconstructed for the fibroadenoma is ≈0.03 cm$^{-1}$ at 830 nm, corresponding to an ICG concentration of ≈0.06 mg/liter. The full-width at half-maximum size of the lesion appears underestimated. Such differences may be partly attributed to the different distribution mechanisms of ICG and Gd-DTPA, as explained in the discussion section, and partly to the low DOT resolution. No other structure significantly enhances in this image. The DOT image is printed in scale with Fig. 3*b* for direct comparison between the DOT images.

**Case III: Healthy Tissue.** Fig. 5 depicts the results from the control case: namely, a patient that demonstrated no suspicious enhancement in the post-Gd images. Fig. 5*a* shows an arbitrarily selected sagittal functional image passing from the middle of the breast. Minor signal enhancement attributable to Gd appears (in color) scattered in a random manner throughout the breast (color superposition is also thresholded to 40% of the maximum). Fig. 5*b* shows the result of DOT for the selected volume of interest, in scale with the results of Figs. 3*b* and 4*b*, and Fig. 5*c* depicts the functional coronal MR image produced similarly to Fig. 3*c*. The optical image shows moderate enhancements (≈0.025 cm$^{-1}$) in the left and right sides of the image, which coincide with increased number of enhanced structures seen on the MR coronal slice.

## Discussion

In this paper, we have investigated the fidelity of DOT for imaging the *in vivo* distribution of ICG in human breast by comparing it with MRI. The Gd-enhanced MR images provide insight on the func-

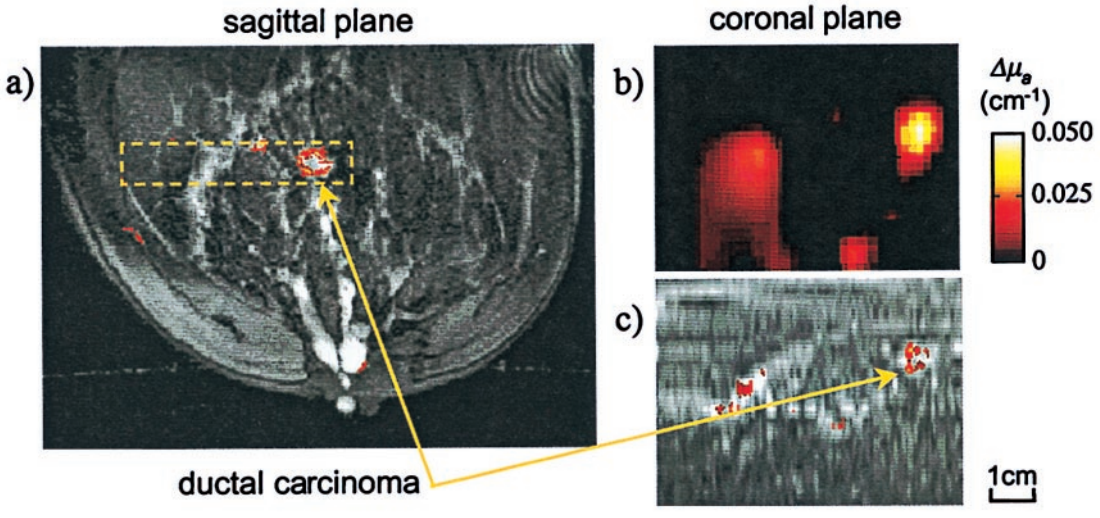


**Fig. 3.** Case I: Ductal carcinoma. (*a*) Functional sagittal MR image after Gd contrast enhancement passing through the center of the cancerous lesion. (*b*) Coronal DOT image, perpendicular to the plane of the MRI image in *a*, for the VOI indicated on *a* with the interrupted line box. (*c*) Functional MR coronal reslicing of the VOI with the same dimensions as *b*.

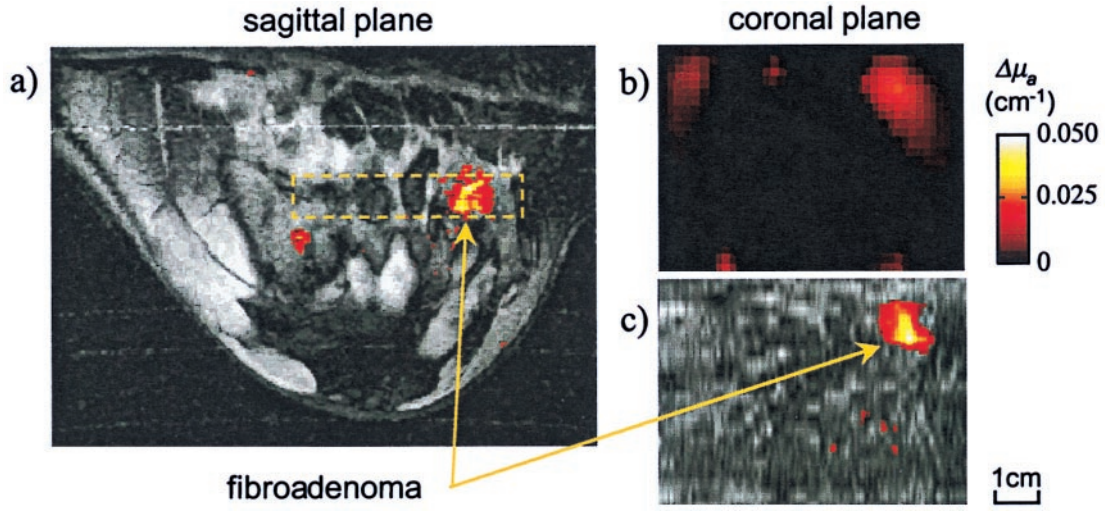


**Fig. 4.** Case II: Fibroadenoma. (*a*) Functional sagittal MR image after Gd contrast enhancement passing through the fibroadenoma. (*b*) Coronal DOT image, perpendicular to the plane of the MRI image in *a*, for the VOI indicated on *a* with the interrupted line box. (*c*) Functional MR coronal reslicing of the VOI with the same dimensions as *b*.

tional characteristics of lesions and supported by the histopathological findings serve as our Gold Standard.

In the case of the carcinoma (Case I), the optical method resolves two lesions that are congruent with the two primary areas that enhance after Gd administration. The accuracy of this localization is within the resolution limits allowed by the reconstruction mesh (≈4 mm). A good correlation is also seen between the contrast of the imaged lesions: the enhancement intensity of the carcinoma relatively to the secondary lesion is ≈2:1 for the two modalities. This contrast consistency can be attributed to the fact that both ICG and Gd are expected to be probes of hypervascularization in this study, even though they have different distribution patterns. Gd are known as extracellular agents that quickly distribute in the intravascular space and the whole body interstitial space [except in the central nervous system (41)]. Hence, cancer differentiation caused by Gd is mainly attributed to the hypervascularity of cancers (42, 43). On the other hand, when ICG is injected in the blood stream, it binds immediately and totally to blood proteins, primarily albumin by 95%, but also $\alpha$-1-lipoproteins and $\beta$-1-lipoproteins (31, 44). Therefore, it is likely that ICG does not significantly extravagate except for incidences of abnormal blood capillaries with high permeability, as in the case of tumor hypervascularity (45). This extravagation would be a slow process, as has been suggested by studies of similar macromolecular contrast agents such as the albumin-bound-Gd molecule (46). Under this premise, only minimum ICG extravagation should occur 3 min after injection (when the optical images were acquired). The coronal slices of Fig. 3 *b* and *c* could then be seen approximately as vascularization maps, with the carcinoma in this case being two times more vascular compared with the secondary benign lesion.

In the case of the fibroadenoma (Case II), the moderate ICG enhancement similarly indicates lower vascularization. The MR diagnosis in this protocol does not use quantified information; the characterization of the lesion is based on morphological features, such as lobulated borders and internal septations. Therefore, MRI enhancements seen in different patients are not compared with

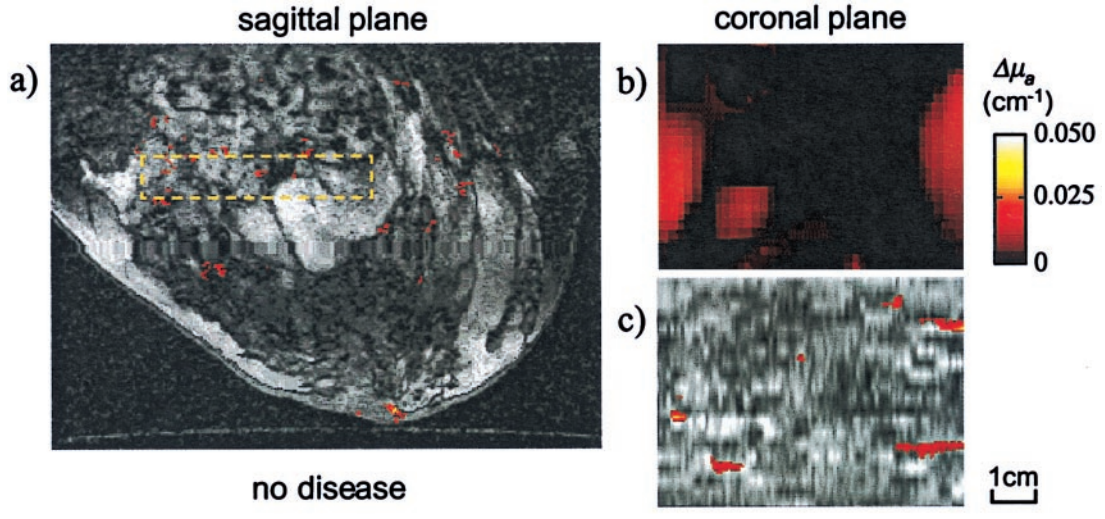


**Fig. 5.** Case III: No disease. (*a*) Functional sagittal MR image after Gd contrast enhancement passing through the middle plane of the breast. (*b*) Coronal DOT image, perpendicular to the plane of the MRI image in *a*, for the VOI indicated on *a* with the interrupted line box. (*c*) Functional MR coronal reslicing of the VOI with the same dimensions as *b*.

each other on an intensity basis. The use of quantified information, however, seems to be an important feature for DOT diagnosis, which by construction produces quantitative images of the absorption coefficient in this study.

Finally, in the normal case, the several minor enhancements shown on the MR coronal slice (Fig. 5*c*) are caused by distributed small vascular structures. Healthy breast demonstrates a heterogeneous ICG distribution, probably similar to the Gd enhancement pattern seen in this measurement. Hence, the reconstruction of the large absorbing lesions at the sides of Fig. 5*b* reflects an average absorption increase caused by many small-localized centers that cannot be adequately resolved independently, as was also observed in the reconstruction of the secondary benign lesion in Fig. 3*b*.

Although it is not feasible in this study to validate the accuracy of the reconstructed $\mu_a$, by keeping the reconstruction parameters similar in the three cases examined, it is shown that quantification could be used diagnostically or as a probe of functionality. This is a significant advantage over transillumination. The evaluation of ICG as a contrast agent of high diagnostic potential requires a larger patient study. Our findings suggest that ICG, although not developed as a cancer targeting dye, could find applications in DOT mammography. Additionally, it should be pointed out that the study of macromolecular contrast agent kinetics enables the independent estimation of vascularization and permeability (47–49). Such differentiation has been demonstrated by MRI using albumin-bound-Gd and is examined by the MR community as a surrogate to increasing specificity (47, 50, 51). In this study, the time-limitations of our protocol did not allow imaging at longer times after ICG injection. However, images taken at later times could study localized ICG kinetics and thus quantify permeability as well, offering an additional feature for cancer differentiation.

Independently of the ICG performance in breast cancer detection, however, DOT has been shown to be capable of localizing and quantifying enhancing lesions *in vivo.* Hence, it could be used to investigate the clinical utility of different contrast agents and use the best of them for optical mammography. In support of this view is the fact that the diagnostic mechanisms of DOT do not focus on high-resolution structural details but rather on local functional characteristics. Furthermore, the resolution and sensitivity of DOT is expected to increase by increasing the source-detector pairs employed and the signal-to-noise ratio. Finally, the use of appropriate NIR markers developed to target specific biological or molecular properties of tissue may expand the potential applications of DOT in probing functionality.

As can be seen in Fig. 1, the optical protocol aims at imaging both the intrinsic and extrinsic breast optical contrast. However, we have chosen not to present images of the intrinsic contrast here, to keep the presentation concise and focus on issues related with imaging of the ICG distribution. Furthermore, the coregistration of the two contrast agents has provided a very good comparison model for the validation of the technique. The results of intrinsic contrast should appear in a follow-up report in which all of the specific inferences pertaining to the imaging of the intrinsic contrast could be analytically presented.

We are grateful to Thomas Connick for the construction of the RF coils and the help in coupling the optical system into the MR scanner; to Norman Butler, Tanya Kurtz, Doris Cain, Jean McDermott, and Lori Pfaff for their invaluable assistance with patient scheduling, management and consent; and to XuHui Ma for his help with the data collection. We acknowledge support for this work from National Institutes of Health Grants ROI CA60182 and ROI-CA75124.

1. Arridge, S. R (1995) *Appl. Opt.* **34,** 7395–7409.
2. O'Leary, M. A., Boas, D. A., Chance B. & Yodh, A. G (1995) *Opt. Lett.* **20,** 426–428.
3. Jiang, H., Paulsen K. D., Osterberg U. L., Pogue, B. W. & Patterson, M. S. (1996) *J. Opt. Soc. Am. A* **13,** 253–266.
4. Gonatas, C. P., Ishii, M., Leigh, J. S. & Schotland, J. C. (1995) *Phys. Rev. E* **52,** 4361–4365.
5. Chang, J. H., Graber, H. L. & Barbour, R. L. (1997) *IEEE T Bio. Med. Eng.* **44,** 810–822.
6. Sevick-Muraca, E. M., Lopez, G., Reynolds, J. S., Troy T. L. & Hutchinson C. L. (1997) *Photochem. Photobiol.* **66,** 55–64.
7. O'Leary, M. A., Boas, D. A., Li, X. D., Chance, B. & Yodh, A. G. (1996) *Opt. Lett.* **21,** 158–160.
8. Sevick, E. M., Chance, B., Leigh, J., Nioka, S. & Maris, M. (1991) *Anal. Biochem.* **195,** 330–351.
9. Beauvoit, B., Kitai, T. & Chance, B. (1994) *Biophys. J.* **67,** 2501–2510.
10. Vaupel, P, Thews, O, Kelleher, D. K., Hoeckel, M. (1998) *Oxygen Transport to Tissue XX* **454,** 591–602.
11. Hopak, E. R., Leek, R., Klenk, N., Lejeune, S., Smith, K., Stuart, N., Greenall, M., Stepniewska, K. & Harris, A. L. (1992) *Lancet* **340,** 1120–1124.
12. Vaupel, P. (1997) *Adv. Exp. Med. Biol.* **411,** 243–254.
13. Virllinger, A. & Chance, B. (1997) *Trends Neurosci.* **20,** 435–442.
14. Nioka, S., Moser, D., Lech, G., Evengelisti, M., Verde, T., Chance, B. & Kuno, S. (1998) *Oxygen Transport to Tissue XX* **454,** 63–70.
15. Gopinath, S. P., Robertson, C. S., Grossman, R. G. & Chance B. (1993) *J. Neurosurg.* **79,** 43–47.
16. Cutler, M. (1929) *Surg. Gynecol. Obstet.* **48,** 721–729.
17. Watmough, D. J. (1983) *Radiology* **147,** 89–92.
18. Sickles, E. A. (1984) *Am. J. Roentgenol.* **142,** 841–844.
19. Wallberg, H., Alveryd, A., Bergvall, U., Nasiell, K., Sundelin P. & Troel, S. (1985) *Acta Radiol. Diagn.* **26,** 33–44.
20. Profio, A. E. & Navarro G. A. (1989) *Med. Phys.* **16,** 60–65.
21. Franceschini, M. A., Moesta, K. T., Fantini, S., Gaida, G., Gratton, E., Jess, H., Mantulin, W. W., Seeber, M., Schlag, P. M. & Kaschke, M. (1997) *Proc. Natl. Acad. Sci. USA* **94,** 6468–6473.
22. Grosenick, D., Wabnitz, H., Rinneberg, H. H., Moesta, T. & Schlag, P. M. (1999) *Appl. Opt.* **38,** 2927–2943.
23. Singer, J. R., Grunbaum, F. A., Kohn, P. D.& Zubelli, J. P. (1990) *Science* **24,** 990–993.
24. Schotland, J. C., Haselgrove, J. C. & Leigh, J. S. (1993) *Appl. Opt.* **32,** 448–453.
25. Pogue, B. W., Testorf, M., McBride, T., Osterberg, U. & Paulsen, K. (1997) *Opt. Express* **1,** 391–403.
26. Ntziachristos, V., Ma, X. H. & Chance, B. (1998) *Rev. Sci. Instrum.* **69,** 4221–4233.
27. Colak, S. B., Papaioannou, D. G., Hooft, G. W., vander Mark, M. B., Schomberg, H., Paasschens, J. C. J., Melissen, J. B. M., van Asten, N. A. A. J. (1997) *Appl. Opt.* **36,** 180–213.
28. Walker, S. A., Fantini, S., Gratton, E. (1997) *Appl. Opt.* **36,** 170–179.
29. Jiang, H. B., Paulsen, K. D., Osterberg, U. L. & Patterson, M. S. (1998) *Phys. Med. Biol.* **43,** 675–693.
30. Hebden, J. C., Schmidt, F. E. W, Fry, M. E., Schweiger, M., Hillman, E. M. C., Delpy, D. T. & Arridge, S. R. (1999) *Opt. Lett.* **24,** 534–536.
31. Cherrick, G. R, Stein, S. W., Leevy. C. M. & Davidson C. S. (1960) *J. Clin. Invest.* **39,** 592–600.
32. Ntziachristos, V., Chance, B. & Yodh, A. G. (1999) *Optics Express* **5**(10), 230–242.
33. Barbour, R. L., Graber, H. L., Chang, J. W., Barbour, S. L. S., Koo P. C. & Aronson R. (1995) *IEEE Comp. Sci. Eng.* **2,** 63–77.
34. Ntziachristos, V., O'Leary, M., Chance B. & Yodh A. G. (1996) *OSA TOPS on Advances in Optical Imaging and Photon Migration* **2,** 164–168.
35. Kak, A. C. & Slaney, M. (1988) *Principles of Computerized Tomographic Imaging* (IEEE, New York), pp. 208–218.
36. Patterson M. S., Chance, B. & Wilson B. C. (1988) *Appl. Opt.* **28,** 2331–2336.
37. Herman, G. T., Lent, A. & Rowland, S. (1973) *J. Theor. Biol.* **43,** 1–32.
38. Insko, E. K., Connick, T. J., Schnall, M. D. & Orel, S. G. (1997) *Magn. Reson. Med.* **37,** 778–784.
39. Ntziachristos, V., Ma, X. H., Yodh, A. G. & Chance, B. (1999) *Rev. Sci. Instr.* **70,** 193–201.
40. Fishkin, J. B. & Gratton, E. (1993) *J. Opt. Soc. Am. A.* **10,** 127–140.
41. Rosen, B. R., Belliveau, J. W., Buchbinder, B. R., McKinstry, R. C., Porkka, L. M., Kennedy, D. N., Neuder, M. S., Fisel, C. R., Aronen, J. J., Kwong, K. K., *et al.* (1991) *Magn. Reson. Med.* **19,** 285–292.
42. Buadu, L. D., Murakami, J., Murayama, S., Hashiguchi, N., Sakai, S., Masuda, K., Toyoshima, S., Kuroki, S. & Ohno, S. (1996) *Radiology* **200,** 639–649.
43. Heywang-Kobrunner, S. H. (1994) *Invest. Radiol.* **29,** 94–104.
44. Paumgartner, P., Probst, P., Kraines, R. & Leevy, C. M. (1970) *Ann. N.Y. Acad. Sci.* **170,** 134–147.
45. Hansen, D. A., Spence, A. M., Carski, T. & Berger, M. S. (1993) *Surg. Neurol.* **40,** 451–456.
46. Su, M. Y., Najafi, A. A. & Nalcioglou, O. (1995) *Magn. Reson. Med.* **34,** 402–411.
47. van Dijke, C. F., Brasch, R. C., Roberts, T. P., Weidner, N., Mathur, A., Shames, D. M., Mann, J. S., Demsar, F., Lang, P. & Schwickert, H. C. (1996) *Radiology* **198,** 813–818.
48. Schwickert, H. C., Stiskal, M., van Dijke, C. F., Roberts, T. P., Mann, J. S., Demsar, F. & Brasch, R. C. (1995) *Acad. Radiol.* **2,** 851–858.
49. Demsar, F., Roberts, T. P. L., Schwickert, H. C., Shames, D. M., van Dijke, C. F., Mann, J. S., Saeed, M. & Brasch, R. C. (1997) *Magn. Reson. Med.* **37**, 236–242.
50. Daldrup, H., Shames, D. M., Wendland, M., Okuhata, Y., Link, T. M., Rosenau, W., Lu, Y. & Brasch, R. C. (1998) *Am. J. Roentgenol.* **171,** 941–949.
51. Adam, G., Muhler, A., Spuntrup, E., Neuerburg, J. M., Kilbinger, M., Bauer, H., Fucezi, L., Kupper, W. & Gunther, R. W. (1996) *Invest. Radiol.* **31,** 267–274.